

# Atomically Flat Zigzag Edges in Monolayer MoS<sub>2</sub> by Thermal Annealing

Qu Chen,<sup>†</sup> Huashan Li,<sup>‡</sup> Wenshuo Xu,<sup>†</sup> Shanshan Wang,<sup>‡</sup> Hidetaka Sawada,<sup>†,§,||</sup> Christopher S. Allen,<sup>†,||</sup> Angus I. Kirkland,<sup>†,||</sup> Jeffrey C. Grossman,<sup>‡</sup> and Jamie H. Warner<sup>\*,†,||</sup>

<sup>†</sup>Department of Materials, University of Oxford, Parks Road, Oxford, OX1 3PH, United Kingdom

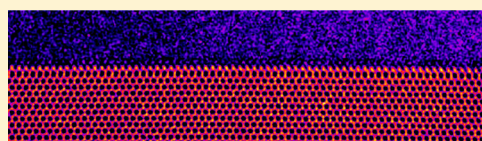
<sup>‡</sup>Department of Materials Science and Engineering, Massachusetts Institute of Technology, 77 Massachusetts Avenue, Cambridge, Massachusetts 02139, United States

<sup>§</sup>JEOL Ltd., 3-1-2 Musashino, Akishima, Tokyo 196-8558, Japan

<sup>||</sup>Electron Physical Sciences Imaging Center, Diamond Light Source Ltd., Didcot, Oxfordshire, OX11 0DE, United Kingdom

## S Supporting Information

**ABSTRACT:** The edges of 2D materials show novel electronic, magnetic, and optical properties, especially when reduced to nanoribbon widths. Therefore, methods to create atomically flat edges in 2D materials are essential for future exploitation. Atomically flat edges in 2D materials are found after brittle fracture or when electrically biasing, but a simple scalable approach for creating atomically flat periodic edges in monolayer 2D transition metal dichalcogenides has yet to be realized. Here, we show how heating monolayer MoS<sub>2</sub> to 800 °C in vacuum produces atomically flat Mo terminated zigzag edges in nanoribbons. We study this at the atomic level using an ultrastable in situ heating holder in an aberration-corrected transmission electron microscope and discriminating Mo from S at the edge, revealing unique Mo terminations for all zigzag orientations that remain stable and atomically flat when cooling back to room temperature. Highly faceted MoS<sub>2</sub> nanoribbon constrictions are produced with Mo rich edge structures that have theoretically predicted spin separated transport channels, which are promising for spin logic applications.



**KEYWORDS:** MoS<sub>2</sub>, TEM, edges, 2D materials, in situ heating, transition metal dichalcogenides

Monolayer MoS<sub>2</sub> has a direct band gap with semiconducting properties for potential applications in electronics and optoelectronics. Edge terminations of 2D materials, such as graphene and TMDs, have been explored theoretically and experimentally,<sup>1–5</sup> with predicted metallic states that cross the bulk energy gap along MoS<sub>2</sub> or WS<sub>2</sub> zigzag edges.<sup>2,6–9</sup> These edge states can be magnetic,<sup>7</sup> induce 1D plasmonic excitations,<sup>10</sup> exhibit high catalytic activity,<sup>11–14</sup> and show increased photoluminescence emission and nonlinear optical responses.<sup>15,16</sup> The influence of the MoS<sub>2</sub> edge structure is key to realizing the idealized electronic and magnetic properties of MoS<sub>2</sub> nanoribbons, which have been predicted to be promising candidates not only for nanoelectronics,<sup>7,9,17,18</sup> but also for hydrogen evolution reaction (HER),<sup>19</sup> and the cathode material of Li-ion batteries due to the enhanced binding between MoS<sub>2</sub> edges and Li without deterioration of Li mobility.<sup>20</sup> Theoretical studies for MoS<sub>2</sub> indicate an energetic preference for zigzag terminations.<sup>2,3,5,21,22</sup>

Heating 2D crystals in reactive gases causes etching along preferential lattice directions, but little is known about the resultant edge roughness at the atomic level. Recent attention has been directed to the atomic structure of edge terminations in graphene and hBN, with few images of TMD edges reported.<sup>23</sup> Aberration-corrected transmission electron microscopy (AC-TEM) enables the direct imaging of atomic structure in 2D materials and can resolve edge terminations. Annular

dark field scanning transmission electron microscopy (ADF-STEM) provides Z-dependent contrast to discriminate Mo and S columns in MoS<sub>2</sub> based on their difference in atomic mass, necessary for evaluating the details of the edge terminations.<sup>24,25</sup>

Here, we show how heating monolayer MoS<sub>2</sub> (Figure S1) in vacuum leads to atomically flat zigzag edges, studied using an in situ heating holder (Figure 1g and h). The electron beam is blanked until the sample reaches 800 °C (Figure 1f), ensuring hydrocarbon removal (Figures S2 and S3). Edges of holes within the MoS<sub>2</sub> sample increase in size with electron beam irradiation at 60 kV due to sulfur vacancies migrating to the edge (Figure S4). Two types of atomically flat zigzag edges are found (Figure 1a) associated with the hexagonal symmetry of monolayer MoS<sub>2</sub>; (10 $\bar{1}$ 0) Mo and ( $\bar{1}$ 010) S, as indicated with blue and yellow lines in Figure 1a. The Mo-edge is the energetically favored termination when compared to the S-edge.<sup>9,22</sup> Atomically flat edges along both zigzag directions (Figure 1b and d) have average and maximum lengths of ~12 and 25 nm, respectively (Figure 1i) and different atomic terminations. At higher temperature (800 °C) S vacancies migrate faster (Figure S5) during imaging but can still be

**Received:** May 24, 2017

**Revised:** July 25, 2017

**Published:** August 11, 2017

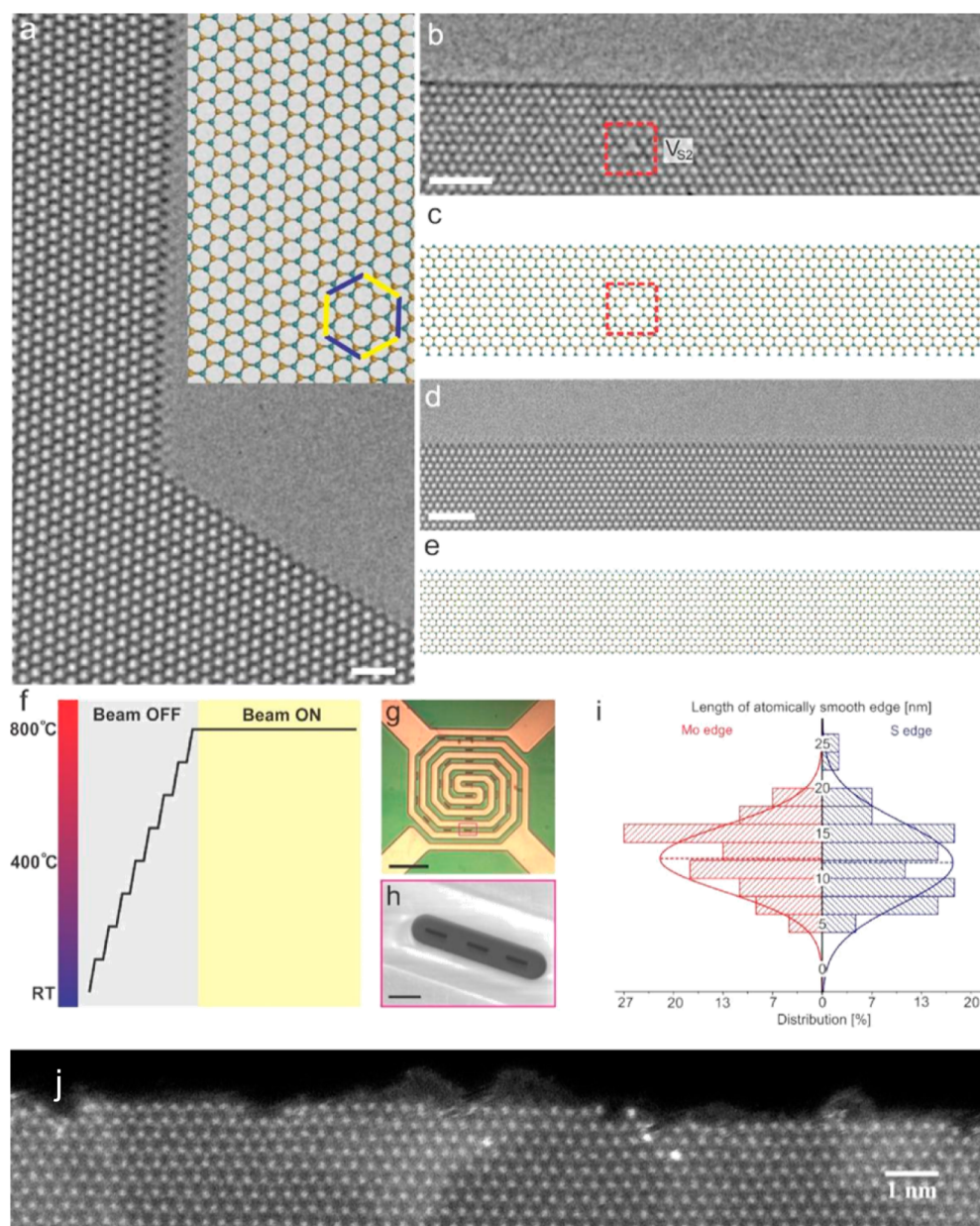


**Figure 1.** AC-TEM images recorded at 800 °C showing atomically flat edges in monolayer MoS<sub>2</sub>. (a) AC-TEM image of a joint of two types of zigzag edges, with inset an atomic model showing the lattice orientation and the zigzag directions (yellow lines for S-edge and blue lines for Mo-edges). (b) AC-TEM image of a Mo edge, with the presence of a disulphur vacancy (V<sub>S2</sub>) highlighted by a red dashed box. (c) Corresponding atomic model for the Mo edge in panel b, cyan balls represent Mo and gold balls 2S. (d) AC-TEM image of a S-edge. (e) Atomic model corresponding to d. (f) Temperature profile and electron beam conditions for the production of long MoS<sub>2</sub> edges. (g) Optical image of the in situ heating chip serving as the supporter and heating device for MoS<sub>2</sub> domains. (h) SEM image of the detailed structure for one slit (highlighted in magenta box in g) in the heating chip. Further details of the equipment are given in [Supporting Information](#). (i) Length distributions of atomically flat Mo- and S-edges. Scale bars in (a) = 1 nm, (b and d) = 2 nm, (g) = 0.1 mm, (h) = 5 μm. (j) Room temperature ADF-STEM image of the edge of a MoS<sub>2</sub> domain showing atomic corrugations.

occasionally detected ([Figure 1b](#) and [Movie S1](#)).<sup>26,27</sup> This enables the discrimination between Mo and S sites within the hexagonal lattice in phase contrast images, which can then be tracked to the edge to determine the edge orientations. The edges of MoS<sub>2</sub> domains at room temperature typically have atomic level terracing and corrugations ([Figure 1j](#)) and lack the atomic flatness seen at high temperatures ([Figure 1b](#) and d).

ADF-STEM was used to determine the position of Mo and S atoms in reconstructed edges based on the difference in Z number. Mo has  $Z = 42$ , and 2S has  $Z = 32$ , which means the Mo has higher contrast than the 2S column in the ADF-STEM

image. ([Figure 2](#)) (gray scale ADF-STEM image in [Figure S6](#)). The structure of the Mo edge [(10 $\bar{1}0$ ) Mo] shown in [Figure 2a](#) was predicted by density functional theory (DFT) and previously observed by scanning tunnelling microscopy and ADF-STEM.<sup>2,3,21,23,28</sup> The edges along the (10 $\bar{1}0$ ) S direction ([Figure 2b](#)) have Mo atoms substituting at 2S positions, leading to Mo termination for all edges in the sample. An intermediate state that rapidly transforms is occasionally observed in small edges before this Mo terminated reconstruction occurs ([Figure S7](#)). This is attributed to the rapid migration of S vacancies to the edge, leading to Mo rich edges (the single S vacancy

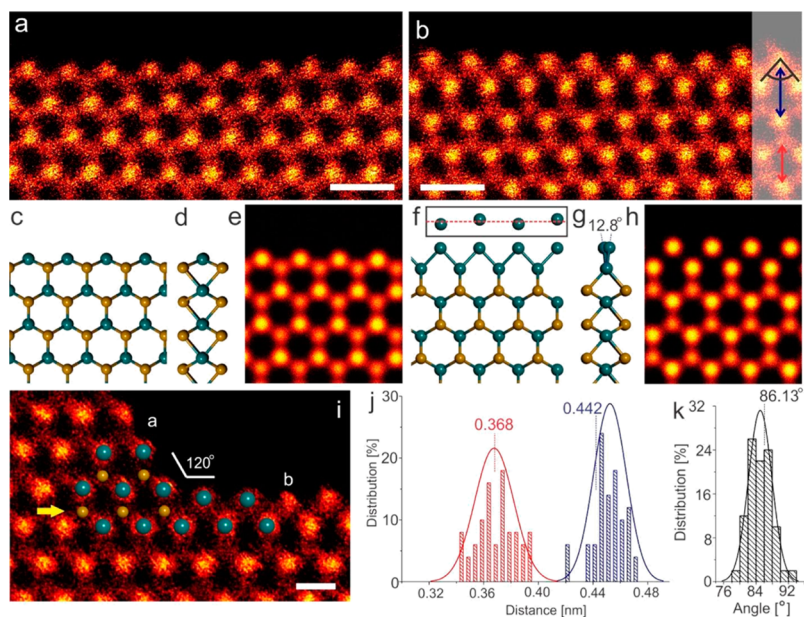


**Figure 2.** (a, b) ADF-STEM images of a Mo edge and Mo-replaced S edge. (c, d) Top and side view of the atomic model of a Mo edge calculated using DFT. (e) Image simulation of the model in c. (f, g) Top and side view of the DFT model of a Mo-replaced S edge, with the black box showing the out-of-plane distortion of the outmost Mo atoms (Red dashed line corresponds to the center of the MoS<sub>2</sub> lattice plane). (h) Image simulation of the model in f. (i) False colored ADF-STEM image of a joint between a Mo-edge and S-edge; letters a and b correspond to the same edge structures shown in panels a and b. Cyan and gold balls represent Mo and 2S sites, respectively. The yellow arrow indicates a line of 2S atoms which are absent at the beginning of the Mo-replaced S edge. (j) Diameter distributions based on experimental data of the 6-atom ring in projection at the Mo-replaced S edge compared to the normal 6-atom ring in MoS<sub>2</sub> lattice, which are  $0.452 \pm 0.012$  nm and  $0.368 \pm 0.014$  nm, respectively. DFT calculated values are 0.442 and 0.368 nm, respectively. (k) Distribution of Mo–Mo–Mo angles based on experimental data:  $85 \pm 3^\circ$  ( $86.1^\circ$  theoretically). Scale bars in (a–b) = 0.5 nm, (i) = 0.3 nm.

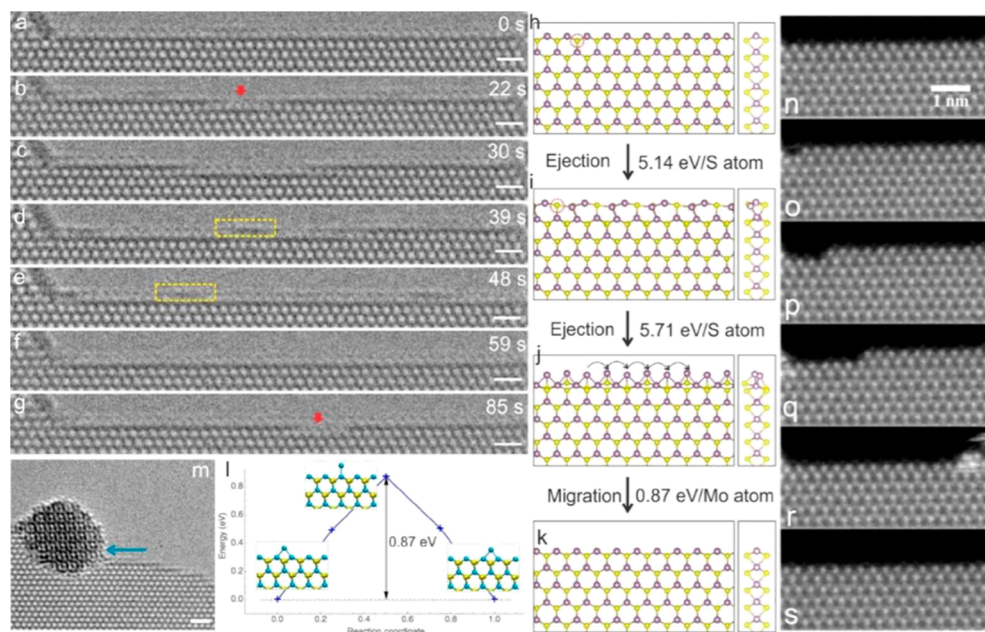


**Figure 3.** In situ observation of layer-by-layer etching along edges and the mechanism predicted by DFT calculations. (a–g) AC-TEM image sequence showing the etching of the outermost layer of a Mo edge. Red arrows indicate the position of the opened breach, and the yellow dashed boxes highlight atoms migrating along the edge. (h–k) Step-by-step etching and reconstruction of the Mo edge based on DFT calculations including both atom ejection and migration. The red dashed circles highlight the position of one example of an ejected S atom. (l) Minimum energy path for a Mo atom migrating between two low energy states. (m) Mo nanocrystal formed by migrating Mo atoms. Time series of ADF-STEM images showing etching along a double Mo terminated edge.

diffusion barrier is 2.33 eV). The intersection of both zigzag edge directions highlights the different Mo terminations (Figure 2i, Figure S7b). The edge reconstruction induces a

22% elongation (20% theoretically) in comparison to the bulk (Figure 2j and k). DFT calculations indicate that the outermost Mo atoms have an energetically favorable (0.056 eV) out-of-

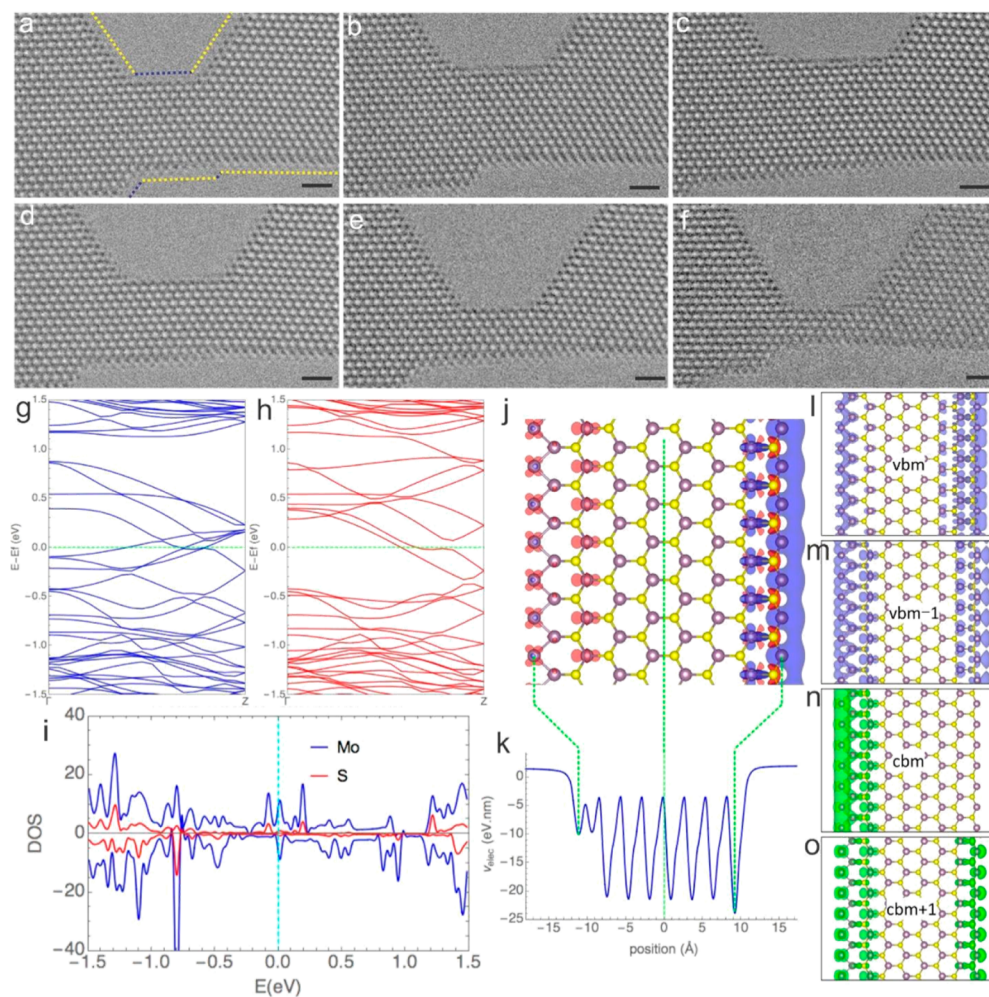


**Figure 4.** Atomic structure of a MoS<sub>2</sub> nanoribbon and DFT calculated properties. (a–f) AC-TEM image sequence of a MoS<sub>2</sub> nanoribbon showing initial widening followed by narrowing. Time duration, 15 s. (g) Spin-up and (h) spin-down band structure of the MoS<sub>2</sub> nanoribbon shown in panel j, with one Mo-replaced S edge (left) and opposite a bare Mo edge. (i) DOS of the MoS<sub>2</sub> nanoribbon with the upper region (positive *y* axis) showing spin-up and the lower region (negative *y* axis) showing spin-down. (j) Spatial distribution of the charge difference between spin-up (blue) and spin-down (red) states for the nanoribbon. (k) Electrostatic potential profile across the nanoribbon in panel j. Each minimum is associated with a line of Mo atoms, and the zero position corresponds to the center of ribbon. (l–o) Wave functions for states around the Fermi level. Scale bars in a–f = 1 nm.

plane distortion (Figure 2f and g). Most importantly, the atomically sharp zigzag edges are maintained after cooling back to room temperature (Figure S8) and can only be disrupted by extensive electron beam irradiation.

The atomically flat edges are formed by a layer-by-layer etching process (Figure 3a–g) starting from a single point (Figure 3 and Movie S2), followed by gradually atom-by-atom removal toward both directions until the entire atomic row is removed before repeating this process (Figure 3g) in similar fashion edge growth in graphene.<sup>29</sup> Some transient contrast arising from Mo migration along the edge during image acquisition is also observed (Figure 3d and e). The melting point of monolayer MoS<sub>2</sub> (~3700 K)<sup>30</sup> exceeds that in our experiment (1073 K), but the weaker bonding of edge atoms may increase their mobility below the melting point. However, the etching process is heavily influenced by electron beam irradiation, supported by theoretical calculations (Figure 3h–l). The edge S atoms are first ejected by the electron beam (Figure 3h to j) due to their higher sputtering cross section leading to bonding between rows of Mo atoms (Figure 3j). A 60–80 keV electron beam is not sufficient to sputter Mo atoms but can

activate edge migration (~0.87 eV) (Figure 3l), leading to agglomeration into Mo-rich crystals (Figure 3m). The Mo-replaced S zigzag edge also etches via a row by row mechanism (Figure 3n–s, S9, and Movie S3).

MoS<sub>2</sub> nanoribbon with the width down to 1–4 nm was first synthesized with the carbon nanotube encapsulation.<sup>31</sup> In our approach, the atom-by-atom etching from the edge also enables fabrication of nanoribbons in MoS<sub>2</sub> with atomically flat edges with different structures on opposite sides (Figure 4a). Etching and atomic migration at the edge of the ribbon occur simultaneously, causing broadening (Figure 4a–c) and narrowing (Figure 4d–f) processes in different local regions (Movie S4). DFT calculations suggest novel electronic and magnetic properties for the MoS<sub>2</sub> nanoribbons (Figure 4g and h), with metallic conductivity according to the band structures shown in Figure 4g and h, which strongly depend on spin type with an intrinsic magnetic moment. The wave functions of states around the Fermi level localize at the ribbon edges as a result of polar discontinuity, implying that the charge transport channels are confined at the edges (Figure 4j). The localization of the spatial distribution of the charge difference between spin-

up and spin-down states reflects the localized nature of the edge states and their responses to a local potential gradient, which may lead to different scattering behavior affecting the transport properties of injected spin at different edges. The magnetic moment for the nanoribbon is  $2.47 \mu_B$ , mainly arising from the d orbitals of Mo edge atoms (Figure S10), which provides a large density of midgap states and substantial splitting. A small contribution from the Mo-replaced S edge may arise from the confinement of bonding orbitals in between two Mo rows, which suppresses spatial redistribution of electron clouds driven by exchange interaction, leading to lower magnetization in comparison to the counterpart double-S atom terminated ribbon ( $3.16 \mu_B$ ) (Figure S11).

The atomically flat edge states created by high temperature annealing may open up the exploration of further quantum phenomena in nanoribbons, such as the Aharonov–Bohm effect, persistent currents, and weak localization.<sup>6,8</sup> The energy levels and exciton binding strength of such edge states can be controlled by modifying the boundary configuration and passivation, resulting in optimization of optical response<sup>15</sup> and catalytic properties. While the intrinsic magnetic moment with ferromagnetic ordering induced by polar discontinuity provides the basis of spintronic devices, the concentration of spin density at nanoribbon edge opens an opportunity to control local resistances and generate transport channels for opposite spin states, which may lead to novel spin logic applications.<sup>32</sup> The scalable processing demonstrated here provides a pathway for creating well-defined atomically precise edges for unambiguous structure–property correlations.

## ■ ASSOCIATED CONTENT

### Supporting Information

The Supporting Information is available free of charge on the ACS Publications website at DOI: 10.1021/acs.nanolett.7b02192.

Description of the MoS<sub>2</sub> synthesis, in situ heating TEM sample preparation, microscopy characterisations, density functional theory calculations, supplementary figures (PDF)

Movie S1: S vacancy migration with S vacancies highlighted in yellow circles (AVI)

Movie S2: Dynamics of etching along Mo edge (AVI)

Movie S3: Layer-by-layer removal of Mo-replaced S edge (AVI)

Movie S4: Narrowing and reconstruction of a MoS<sub>2</sub> nanoribbon (AVI)

## ■ AUTHOR INFORMATION

### Corresponding Author

\*E-mail: [Jamie.warner@materials.ox.ac.uk](mailto:Jamie.warner@materials.ox.ac.uk).

### ORCID

Shanshan Wang: 0000-0003-3750-6737

Jamie H. Warner: 0000-0002-1271-2019

### Notes

The authors declare no competing financial interest.

## ■ ACKNOWLEDGMENTS

J.H.W. is thankful for the support from the Royal Society and the European Research Council.

## ■ REFERENCES

- (1) Zhu, Y. F.; Jiang, Q. *Coord. Chem. Rev.*; Elsevier B.V., 2016; pp 1–33.
- (2) Bollinger, M.; Jacobsen, K.; Nørskov, J. *Phys. Rev. B: Condens. Matter Mater. Phys.* **2003**, *67* (8), 85410.
- (3) Helveg, S.; Lauritsen, J.; Laegsgaard, E.; Stensgaard, I.; Nørskov, J.; Clausen, B.; Topsøe, H.; Besenbacher, F. *Phys. Rev. Lett.* **2000**, *84* (5), 951–954.
- (4) He, K.; Robertson, A. W.; Fan, Y.; Allen, C. S.; Lin, Y.; Suenaga, K.; Kirkland, A. I.; Warner, J. H. *ACS Nano* **2015**, *9* (5), 4786–4795.
- (5) Hansen, L. P.; Ramasse, Q. M.; Kisielowski, C.; Brorson, M.; Johnson, E.; Topsøe, H.; Helveg, S. *Angew. Chem., Int. Ed.* **2011**, *50* (43), 10153–10156.
- (6) Gibertini, M.; Marzari, N. *Nano Lett.* **2015**, *15* (9), 6229–6238.
- (7) Li, Y.; Zhou, Z.; Zhang, S.; Chen, Z. *J. Am. Chem. Soc.* **2008**, *130* (49), 16739–16744.
- (8) Bollinger, M. V.; Lauritsen, J. V.; Jacobsen, K. W.; Nørskov, J. K.; Helveg, S.; Besenbacher, F. *Phys. Rev. Lett.* **2001**, *87* (19), 196803.
- (9) Xiao, S. L.; Yu, W. Z.; Gao, S. P. *Surf. Sci.* **2016**, *653*, 107–112.
- (10) Andersen, K.; Jacobsen, K. W.; Thygesen, K. S. *Phys. Rev. B: Condens. Matter Mater. Phys.* **2014**, *90* (16), 161410.
- (11) Chianelli, R. R.; Siadati, M. H.; De la Rosa, M. P.; Berhault, G.; Wilcoxon, J. P.; Bearden, R.; Abrams, B. L. *Catal. Rev.: Sci. Eng.* **2006**, *48* (1), 1–41.
- (12) Lauritsen, J. V.; Nyberg, M.; Vang, R. T.; Bollinger, M. V.; Clausen, B. S. *Nanotechnology* **2003**, *14* (3), 385–389.
- (13) Jaramillo, T. F.; Jorgensen, K. P.; Bonde, J.; Nielsen, J. H.; Horch, S.; Chorkendorff, I. *Science (Washington, DC, U. S.)* **2007**, *317* (5834), 100–102.
- (14) Lauritsen, J. V.; Bollinger, M. V.; Laegsgaard, E.; Jacobsen, K. W.; Nørskov, J. K.; Clausen, B. S.; Topsøe, H.; Besenbacher, F. *J. Catal.* **2004**, *221* (2), 510–522.
- (15) Gutiérrez, H. R.; Perea-López, N.; Elías, A. L.; Berkdemir, A.; Wang, B.; Lv, R.; López-Urías, F.; Crespi, V. H.; Terrones, H.; Terrones, M. *Nano Lett.* **2013**, *13* (8), 3447–3454.
- (16) Yin, X.; Ye, Z.; Chenet, D. a.; Ye, Y.; O'Brien, K.; Hone, J. C.; Zhang, X. *Science (Washington, DC, U. S.)* **2014**, *344* (6183), 488–490.
- (17) Han, Y.; Zhou, J.; Dong, J. *Appl. Surf. Sci.* **2015**, *346*, 470–476.
- (18) Fan, D. D.; Liu, H. J.; Cheng, L.; Jiang, P. H.; Shi, J.; Tang, X. F. *Appl. Phys. Lett.* **2014**, *105* (13), 133113.
- (19) Liu, L.; Li, X.; Xu, L.-C.; Liu, R.; Yang, Z. *Appl. Surf. Sci.* **2017**, *396*, 138–143.
- (20) Li, Y.; Wu, D.; Zhou, Z.; Cabrera, C. R.; Chen, Z. *J. Phys. Chem. Lett.* **2012**, *3*, 2221.
- (21) Lauritsen, J. V.; Kibsgaard, J.; Topsøe, H.; Helveg, S.; Clausen, B. S.; Laegsgaard, E.; Besenbacher, F. *Nat. Nanotechnol.* **2007**, *2* (1), 53–58.
- (22) Schweiger, H.; Raybaud, P.; Kresse, G.; Toulhoat, H. E. *J. Catal.* **2002**, *207*, 76–87.
- (23) Zhou, W.; Zou, X.; Najmaei, S.; Liu, Z.; Shi, Y.; Kong, J.; Lou, J.; Ajayan, P. M.; Yakobson, B. I.; Idrobo, J. C. *Nano Lett.* **2013**, *13* (6), 2615–2622.
- (24) Krivanek, O. L.; Chisholm, M. F.; Nicolosi, V.; Pennycook, T. J.; Corbin, G. J.; Dellby, N.; Murfitt, M. F.; Own, C. S.; Szilagy, Z. S.; Oxley, M. P.; Pantelides, S. T.; Pennycook, S. J. *Nature* **2010**, *464* (7288), 571–574.
- (25) Nellist, P. D.; Pennycook, S. J. *J. Microsc.* **1998**, *190* (1–2), 159–170.
- (26) Algara-Siller, G.; Kurasch, S.; Sedighi, M.; Lehtinen, O.; Kaiser, U. *Appl. Phys. Lett.* **2013**, *103* (20), 203107.
- (27) Robertson, A. W.; Allen, C. S.; Wu, Y. a.; He, K.; Olivier, J.; Neethling, J.; Kirkland, A. I.; Warner, J. H. *Nat. Commun.* **2012**, *3*, 1144.
- (28) Yu, S.; Zheng, W. *Phys. Chem. Chem. Phys.* **2016**, *18* (6), 4675–4683.
- (29) Warner, J. H.; Rummeli, M. H.; Ge, L.; Gemming, T.; Montanari, B.; Harrison, N. M.; Büchner, B.; Briggs, G. A. D. *Nat. Nanotechnol.* **2009**, *4* (8), 500–504.

(30) Singh, S. K.; Neek-Amal, M.; Costamagna, S.; Peeters, F. M. *Phys. Rev. B: Condens. Matter Mater. Phys.* **2015**, *91* (1), 14101.

(31) Wang, Z.; Li, H.; Liu, Z.; Shi, Z.; Lu, J.; Suenaga, K.; Joung, S. K.; Okazaki, T.; Gu, Z.; Zhou, J.; Gao, Z.; Li, G.; Sanvito, S.; Wang, E.; Iijima, S. *J. Am. Chem. Soc.* **2010**, *132* (39), 13840–13847.

(32) Han, W.; Kawakami, R. K.; Gmitra, M.; Fabian, J. *Nat. Nanotechnol.* **2014**, *9* (10), 794–807.